Microstructure correlated ferromagnetism in manganese stabilized zirconia nanoparticles

Anshuman Nandy [a], Umapada Pal [b], Swapan Kumar Pradhan [c, *]

[a] *Department of Physics, City College, Kolkata, 700009, India*
[b] *Instituto de Física, Benemérita Universidad Autónoma de Puebla, Apdo. Postal J-48, Puebla, Pue, 72570, Mexico*
[c] *Department of Physics, The University of Burdwan, Golapbag, Burdwan, 713104, India*

ARTICLE INFO

ABSTRACT

Pure and 5—30 mol% metallic Mn-alloyed partially as well as fully stabilized cubic zirconia nanoparticles were prepared by 10 h mechanical alloying of monoclinic ZrO_2 and Mn metal powders. Structure and microstructure characterizations of the ball-milled powders were carried out by analyzing respective XRD patterns employing the Rietveld refinement method. It is found that Mn, a transition metal with $[Ar3d^5 4s^2]$ electronic configuration acts as a stabilizing element for the cubic ZrO_2 phase. Lattice parameters, oxygen vacancy, particle size, microstrain and relative phase abundances of monoclinic and cubic phases of ZrO_2 were calculated for all the compounds to elucidate the possible dependence of these parameters on Mn incorporation in ZrO_2 lattice. The magnetic behaviour of the nanoparticles was studied at different temperatures under a wide range of applied magnetic field. Effects of Mn incorporation on the microstructure and magnetic behaviour of zirconia nanoparticles were studied to explain the possible origin of magnetism in undoped monoclinic and Mn-stabilized cubic zirconia nanoparticles.

© 2019 Elsevier B.V. All rights reserved.

1. Introduction

Zirconium dioxide (ZrO_2) can exist in three structural polymorphs: monoclinic (m-), tetragonal (t-) and cubic (c-). Phase transitions from monoclinic to tetragonal to cubic can occur with temperature or by adding suitable dopants. A variety of aliovalent dopants can be used to stabilize the high temperature tetragonal or cubic phase of ZrO_2 at room temperature. Together with different dopants, the three polymorphs of zirconia form an excellent class of materials with very interesting properties such as excellent ionic conductivity, high hardness, high dielectric constant etc. [1]. For these properties, zirconia finds vast applications in solid oxide fuel cells, artificial diamonds, catalysis, oxygen sensing and optical devices [1—3]. Another very interesting yet controversial property exhibited by stabilized zirconia is its room temperature ferromagnetism (RTFM). Zirconia is a wide band gap (~6.0 eV) semiconducting oxide, containing non-magnetic cation. The electronic state of Zr^{+4} is same that of [Kr] with no d electron and thus, it should be non-magnetic. RTFM was also observed in doped semiconducting oxides with non-magnetic cations such as ZnO [4—6],

TiO_2 [7—9], SnO_2 [10—12], etc. The magnetism in these compounds was thought to be dopant induced. In 2005, Coey et al. [13—15] first observed RTFM in undoped HfO_2 thin films free from any impurity and they named it as d^0 ferromagnetism as ferromagnetic behaviour was exhibited by non-d block ions. This led to research on other undoped tetravalent oxides like SnO_2 [16] and TiO_2 [17]. The observed RTFM was reported to be strongly related to the structural defects and dislocations within the material [18—20]. Various kinds of defects such as point defects, surface defects, microstrain and structure defects have been attributed to the RTFM in these semiconducting oxides. Point defects arising from oxygen vacancies and interstitials were found to be mostly responsible for the ferromagnetic behaviour of these oxides. Having similar or even more exotic properties than of HfO_2, TiO_2 and SnO_2, zirconia is expected to show stronger RTFM. This led to a number of theoretical studies on zirconia. In 2007, Ostanin et al. [21] first predicted that Mn-doped cubic ZrO_2 can be a candidate material for diluted magnetic oxides by DFT calculations. This led to other theoretical and experimental works on the magnetism of undoped and transition metal doped zirconia [22—25]. In fact, those efforts triggered a re-examination of the ferromagnetic behaviour of undoped zirconia in m-, t- and c-ZrO_2 polymorphs. Undoped zirconia thin films were found to be ferromagnetic at room temperature, opening up a new

---

venture, i.e. the so-called d^0 ferromagnetism of zirconia [26]. While the results on RTFM behaviours of undoped and metal stabilized zirconia thin films have been presented extensively in the review performed by Ning and Zhang [27], there is no such detailed study yet on cubic zirconia nanoparticles.

As microstructure plays a very important role in regulating the magnetic behaviour of transition metal oxide nanoparticles, a detailed microstructural characterization should precede the magnetic measurements to understand the origin of RTFM in these nanostructures. In our previous works, it was demonstrated that by mechanical alloying, it is possible to synthesize 5–20 mol% Mn-doped or Mn-stabilized cubic ZrO$_2$ nanoparticles [28]. While Mn incorporation does affect the electrical properties, enhancing their ionic conductivity and performance as fuel cell electrolyte material [29,30], incorporation of Mn is also expected to alter the magnetic behaviour of ZrO$_2$ nanoparticles.

In the present study, partially stabilized nanocrystalline cubic zirconia has been synthesized without any dopant by mechanical alloying the analytical grade pure zirconia powder of monoclinic phase (m-ZrO$_2$), similar to previous work [31]. For full stabilization of cubic phase, metallic Mn was added as transition metal dopant. Microstructures of all the Mn-stabilized c-ZrO$_2$ nanoparticles were critically examined by Rietveld refinement of their XRD data. Microstructural parameters of analytical grade undoped and 5–30 mol% Mn-stabilized zirconia nanoparticles synthesized by the mechanical alloying process has been correlated to their magnetic behaviours. We demonstrate that due to short-range ferromagnetic ordering, RTFM can be induced both in undoped and Mn-stabilized zirconia nanoparticles, even though Zr^{+4} is a non-d block element and Mn itself is paramagnetic at room temperature.

2. Material and methods

Analytical grade commercial zirconia powder (m-ZrO$_2$, Loba Chemie, 99.5%) was mechanically milled for 10 h duration in open air with intermediate cooling for 15min after every 15min of milling. Mechanical alloying (MA) was carried out in an 80 ml chrome steel vial with chrome steel balls in a planetary ball mill (model-P5, M/S Fritsch, GmbH, Germany). Pure manganese (Mn, Loba Chemie, 99.8%) and m-ZrO$_2$ powders were taken as starting materials in six different molar ratios of Mn and ZrO$_2$ (i.e. 5:95, 10:90, 15:85, 20:80, 25:75 and 30:70). MA of all the milled samples was carried out under identical experimental conditions (10 h of milling in the air, and 15 min of cooling after every 15 min of alloying). X-ray powder diffraction (XRD) profiles of all the milled powders were recorded in an X'Pert PRO X-ray diffractometer with an accelerator detector (M/S PAN Analytical) using CuK$_\alpha$ radiation in a moist free atmosphere. The XRD step scan data were recorded with a step size of 0.02° within the 2θ range 20° to 70° and a scan rate of 2 s/step. Electron transmission patterns were recorded using a high-resolution transmission electron microscope (HRTEM) (FEI make, FEG TECHNAI 30). A typical SEM (FESEM, JEOL JSM-7800F field-emission scanning electron microscope with attached Oxford Instrument X-Max spectrometer) with 15 KeV accelerating voltage was used for recording Energy-Dispersive X-ray Spectra (EDS) for elemental compositions and mapping. Magnetic measurements of the samples were carried out in a superconducting quantum interface device (SQUID) coupled in DynaCool Physical Properties Measurement System (PPMS) of Quantum Design. Magnetization was recorded against temperature (M-T) and reversible magnetic field (M − H). M-T measurements were carried out in a standard zero fields cooled (ZFC) and field cooled (FC) procedure under a constant magnetic field in the temperature range 1.8 K–380 K with a cooling/heating rate of 2 K/min. The employed slow cooling rate was considered to provide sufficient

time for the spin rearrangement in the samples during low-temperature sintering. M − H measurements were performed under four constant temperatures, two in the very low-temperature range (1.8 K–15 K), one in mid-range (100 K–200 K) and one at room temperature (300 K). M − H measurements were carried out under ±5 T magnetic field with a field variation rate of 100 Oe/min.

Rietveld's powder diffraction profile refinement [32] was performed using MAUD software version 2.26 [33,34] for the structural and microstructural characterization of the prepared nanoparticles. The details of the profile refinement method are discussed elsewhere [31].

3. Results and discussion

3.1. Microstructural characterization

The mechanical alloying process has been employed to prepare the samples for present study, as it is a single step, one-pot synthesis method to incorporate Mn in metallic form and to prepare stabilized cubic zirconia nanoparticles without any high-temperature sintering. The Rietveld refined XRD patterns of analytical grade un-milled commercial ZrO$_2$ (CZ) and 10 h milled pure zirconia powders (PZ) are shown in Fig. 1. It is evident that the CZ is composed only of pure monoclinic zirconia phase, which is exactly simulated with the ICSD file no. 647691 (monoclinic, Sp. Gr. $P2_1/c$, a = 4.67 Å, b = 3.43 Å, c = 5.12 Å, β = 99.3°) with (11-1) as its strongest reflection. In the course of milling, the white zirconia powder transformed slowly to grey nanoparticles after 10 h of MA. The experimental and refined XRD patterns of PZ powder are shown in the upper panel of Fig. 1. Rietveld analysis reveals the growth of nanocrystalline c-ZrO$_2$ phase (~19.15%) which coexists of m-ZrO$_2$ phase (~23.07%) and an amorphous-like c- ZrO$_2$ phase (~57.77%). It was previously reported that mechanical alloying alone can partially stabilize the undoped zirconia in the cubic phase [31]. The authors [31] argued that the process of ball milling exerts shearing stress, which compresses the monoclinic unit cell to cubic unit cell with lesser volume. Other reasons for the phase transformation are the reduction of particle size in the nanometer scale [35] and the creation of oxygen vacancies. XRD patterns of both the crystalline cubic zirconia and the amorphous-like phase were simulated with ICSD file no. 647689 (cubic, Sp. Gr. Fm3m, a = 5.065 Å). Indexed peak positions of both monoclinic and cubic phases are marked in the lower panel of Fig. 1. It is evident that the cubic reflections appear in the XRD pattern with significant peak broadening in the milled compound than the un-milled one. The intensities of all the monoclinic reflections diminished drastically in the milled compound, indicating a rapid reduction of the monoclinic phase in course of milling, in comparison to un-milled powder. It indicates that ~87% cubic phase with extensive peak broadening has been grown with a very small crystallite size and may also contain another kind of lattice imperfections. Rietveld refinement reveals the cubic lattice parameter of PZ is 5.1133 Å and there is a considerable amount of oxygen vacancy in the cubic lattice.

The experimental XRD patterns along with the Rietveld refined outputs of the Mn-stabilized (5–30 mol%) zirconia samples are shown in Fig. 2. With the gradual increase in Mn content, the sample becomes darker (upper panel of Fig. 2). As has been stated earlier, all the samples were prepared by 10 h mechanical alloying with intermediate cooling. A trace amount of un-reacted m-ZrO$_2$ is noticed in the 5 (5MZ), 10 (10MZ) and 15 mol% (15MZ) Mn-stabilized zirconia samples, whereas diffraction peaks associated to metallic Mn appear only in the 25 (25MZ) and 30 mol% (30MZ) Mn-stabilized samples. The sample containing 20 mol% Mn (20MZ) ps formed with single cubic phase, along with an amorphous phase
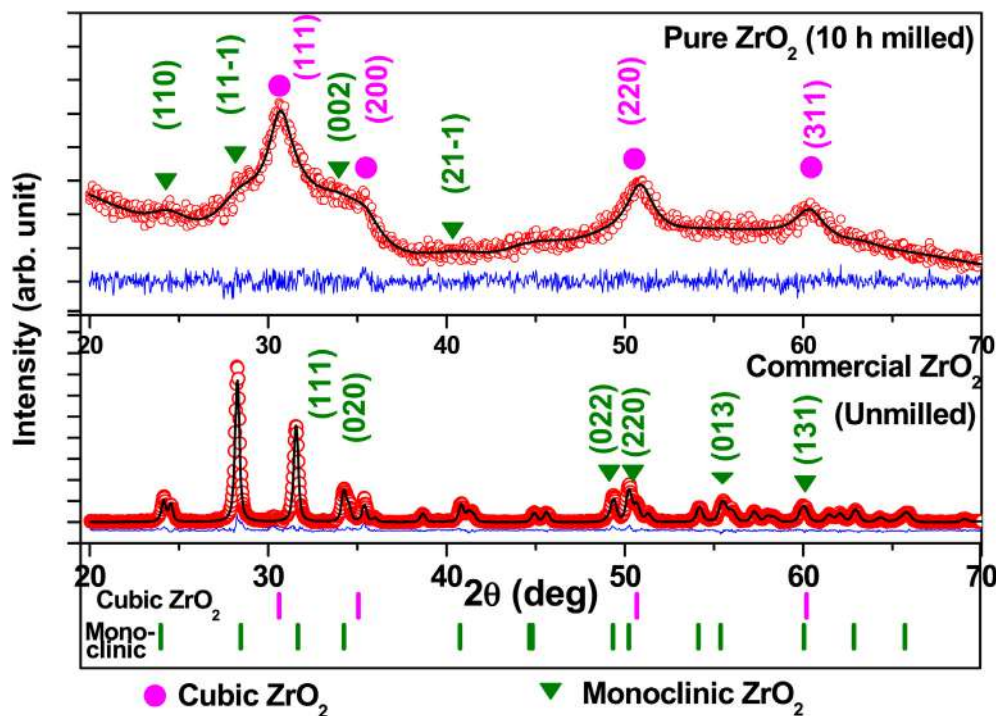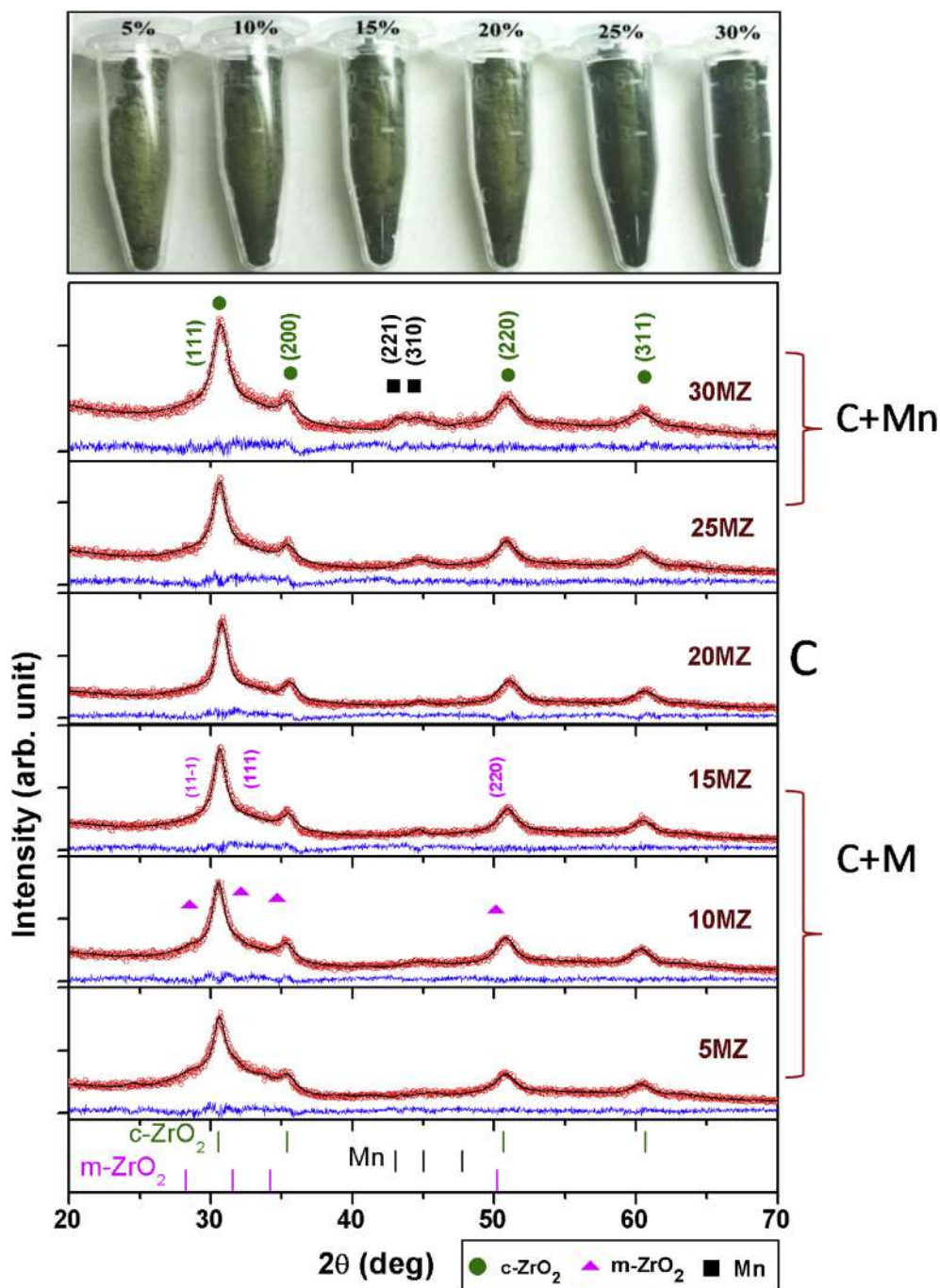
Fig. 1. Typical Rietveld analysis output of the XRD patterns of analytical grade unmilled and 10 h milled ZrO_2 powders. Experimental data are presented as hollow circles and the refined fitted patterns are shown as solid lines through the data points. Solid lines below respective XRD patterns show residues ($I_O - I_C$) between experimental (I_O) and simulated intensities (I_C). Markers show peak positions of the respective phases.

derived from the cubic phase, which is also present in all other samples. The pure metallic Mn phase is simulated with ICSD no. 163411 (cubic, Sp. Gr. $P4_132$, a = 6.315 Å). The insignificant difference between the experimental (I_O) and simulated (I_C) XRD patterns, plotted under respective XRD pattern suggest a good agreement between experimental and simulated intensities for all the samples (Fig. 2). As we have reported earlier [29], both the monoclinic phase and amorphous-like cubic phase can be fully transformed to crystalline cubic phase by sintering the Mn-ZrO$_2$ compounds at a higher temperature, though this will increase the particle size.

Microstructural parameters of the synthesized pure and Mn-stabilized nanoparticles obtained from Rietveld refinements are plotted in Fig. 3. The variations in different phase fractions present in the samples are shown in Fig. 3(a). A gradual decrease in the monoclinic phase with Mn-alloying can be seen, which reduces to 2.4 mol% in 15MZ and completely absent in 20MZ sample. Cubic ZrO$_2$ phase grows with increasing Mn incorporation at the expense of the monoclinic phase. The amorphous like cubic phase also reduces with Mn alloying. This amorphous like phase is very common in the 10 h mechanically alloyed samples, which has been derived from the cubic phase by reducing the particle size and increasing the r.m.s.microstrain. Presence of ~5 and 10 mol% Mn phases is observed in the 25 and 30 mol% Mn-stabilized zirconia samples respectively. It suggests that a maximum of 20 mol% Mn can be incorporated in the zirconia lattice by mechanical alloying. However, we have demonstrated the possibility of ~30 mol% MnO incorporation in zirconia by MA in a previous study [30]. This is because Mn may exist in multi-valent states when alloyed in metallic form with zirconia, whereas when alloyed with MnO, it exists only as Mn^{+2} state. Another reason may be the oxide host lattice is more familiar for an oxide dopant. Fig. 3(b) shows the variation of the lattice parameter and oxygen vacancy in the Mn-

stabilized ZrO$_2$ nanoparticles prepared with different Mn mol%. Both these parameters are estimated from Rietveld refinement. Although during Mn-alloying, Zr^{+4} ions of smaller dimension (radius = 0.84 Å, 8 co-ordinate system) are continuously replaced from their lattice sites by larger Mn^{+2} ions (radius = 0.96 Å, coordination no.8) [36], lattice parameter (left X-axis) of c-ZrO$_2$ decreases gradually up to 20 mol% Mn doping. This indicates the creation and increased association of oxygen vacancies due to Mn doping, which was also seen in some previous reports [28,30,37]. Mn cations are mostly found in +2 valence state from XPS measurements, which were reported earlier [28]. Due to a mismatch in valence states of Mn and Zr ions, increasing Mn incorporation results in increasing oxygen vacancy in the zirconia lattice, in addition to the vacancies already present in the undoped sample. Mn doping decreases the lattice parameter which results into decrease of unit cell volume. Monoclinic to cubic phase transition occurs when the monoclinic unit cell is compressed to cubic unit cell with lesser volume [31]. As can be noticed in Fig. 3(b), the reduction in lattice parameter or the shrinkage of the lattice is well correlated with the increase in oxygen vacancies or vacant positions in the lattice. The changes in the lattice parameter and oxygen vacancy reach their maximum for 20 mol% Mn incorporation and do not alter much thereafter (for 25 and 30 mol% doping), attaining almost their saturation values. The observed results are in good agreement with the solubility limit of Mn, which is nearly 20 mol% in zirconia lattice, as has been demonstrated by phase fraction calculation. On incorporating Mn beyond 20 mol%, the excess Mn remains in metallic phase outside the ZrO$_2$ lattice along with the Mn-stabilized cubic zirconia phase. The variations of crystallite (particle) size and r.m.s.microstrain of all the Mn-stabilized cubic zirconia nanoparticles are shown in Fig. 3(c). The average crystallite sizes of the synthesized zirconia nanoparticles (undoped and Mn-stabilized) remain within 17−19 nm range. A noted decrease in crystallite

Fig. 2. Typical Rietveld analysis output of the XRD patterns of Mn alloyed ZrO_2 compounds. Experimental data are presented as hollow circles and the refined fitted patterns are shown as solid lines through these data points. Solid lines below respective XRD patterns show the residue ($I_O - I_C$) between experimental (I_O) and simulated intensities (I_C). Markers show peak positions of the respective phases. Upper panel shows the actual pictures of the samples.

size up to 20 mol% Mn-alloying is due to an increase in lattice mismatch by continuous Mn substitution with lattice contraction and increase in r.m.s. microstrain in this limit. As the particles are continuously fractured and alloyed during planetary ball milling, microstrain increases up to 20 mol% Mn incorporation. Particle sizes in 25 and 30 mol% Mn-stabilized samples increase slightly due to a small increase in lattice parameter and a decrease in r.m.s. microstrain. The phase formation and shape/size of nanoparticles were also verified with HRTEM images. Some selected HRTEM images of the 20MZ compound are shown in Fig. 4. Co-existence of

both crystalline and amorphous phases is evident in Fig. 4(a). The crystalline planes are identified from interplanar distance measurements and are indexed accordingly. A portion of the purely crystalline region with cubic zirconia phase is shown in Fig. 4(b) with indexed reflecting crystal planes. A single nanoparticle of the compound is shown in Fig. 4(c). The spherical shape of the particle indicates that nanoparticles are isotropic in nature. The measured average particle diameter is well in accordance with the calculated crystallite size of the 20MZ compound as revealed from Rietveld refinement. To study the elemental distribution of Zr, Mn and O
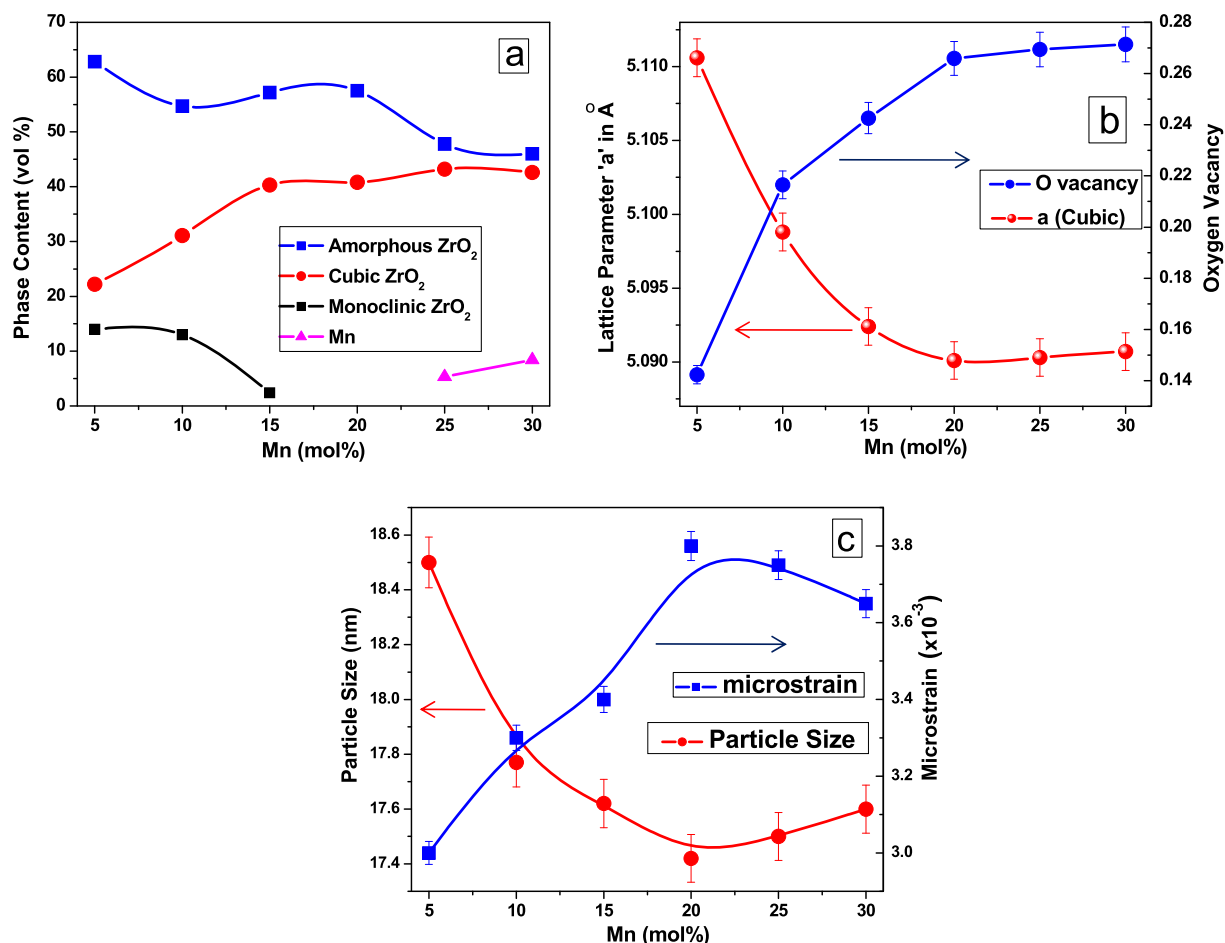
Fig. 3. Variation of (a) phase content (mol%), (b) lattice parameter (left axis) and oxygen vacancy (right axis) of cubic phase and (c) particle size and microstrain of Mn-alloyed cubic zirconia nanoparticles with Mn mol%.
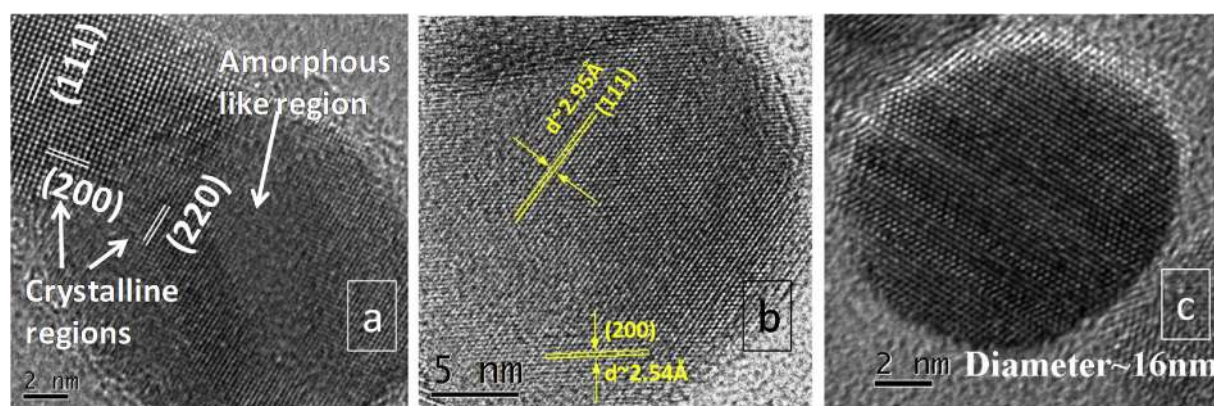
Fig. 4. HRTEM images of 20MZ-(a) Co-existence of crystalline and amorphous phase (b) lattice fringe pattern (c) A single particle.

atoms in the Mn-doped ZrO_2 compounds, the elemental mapping is done by EDS. This is shown in Fig. 5(a) and (b) for 10MZ and 20MZ compounds. As can be seen from these images, all the three elements (Zr, O and Mn) are distributed homogeneously in the nanoparticles. The accurate atomic fractions of incorporated Mn into the ZrO_2 lattice after alloying were measured by EDS analysis and presented in Table 1. The actual atomic fractions are found to very close to the expected composition. Schematic representation of the octahedral arrangement of atoms in cubic ZrO_2 phase present

in Mn stabilized zirconia is shown in Fig. 6. The oxygen vacancy (V_o) created due to the replacement of Zr by Mn is shown by white circles.

3.2. Magnetic characterization

To examine the magnetic behaviours of the analytical grade un-milled commercial zirconia (CZ), 10 h milled pure ZrO_2(PZ) and Mn-stabilized (MZ) zirconia samples, their magnetization data were
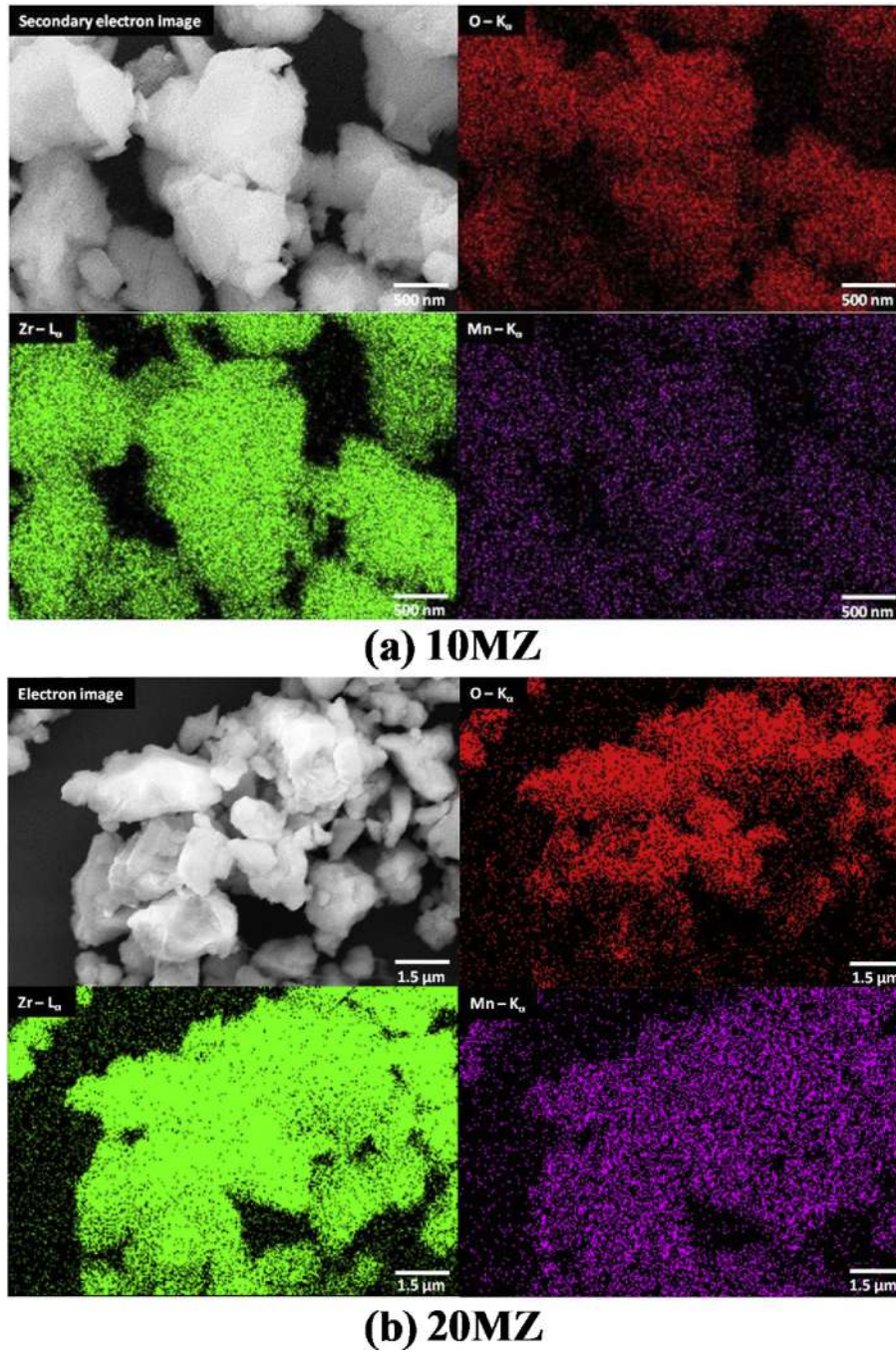
Fig. 5. Elemental mapping by EDS showing O, Zr and Mn distribution for (a) 10MZ (b) 20MZ.

Table 1
Elemental analysis of six compositions of Mn alloyed ZrO_2 after 10 h of mechanical alloying.

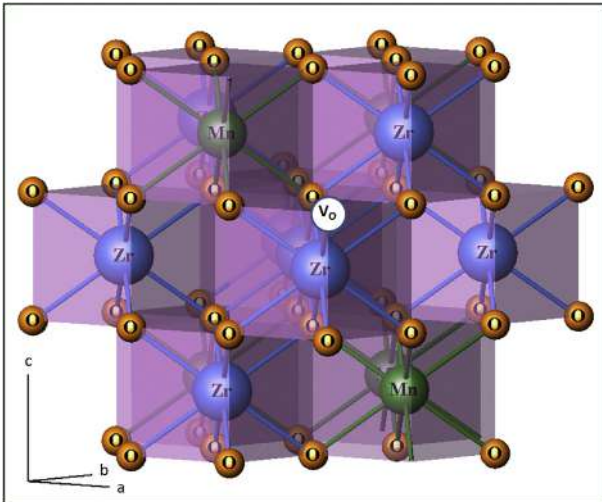| Ingredients taken (mol%)		Elemental analysis (atom%)		
ZrO_2	Mn	Zr	Mn	O
95.0	5.0	23.93	1.20	75.69
90.0	10.0	24.87	2.95	72.19
85.0	15.0	23.98	4.65	71.36
80.0	20.0	22.42	5.87	71.71
75.0	25.0	22.64	8.03	69.33
70.0	30.0	22.49	11.28	66.23

Fig. 6. Octahedral arrangement of atoms in Mn stabilized cubic ZrO_2 compound.

recorded at different temperatures and different applied magnetic fields. The zero-field cooled (ZFC) and field cooled (FC) curves of the un-milled commercial zirconia (CZ) powder recorded applying 500 Oe magnetic field are shown in Fig. 7(a). Like hafnium oxide [38], zirconium oxide is also a wide bandgap (~5.8 eV) material [39], with high (~25) [39] dielectric constant. Like other wide bandgap semiconducting oxides, pure ZrO_2 is diamagnetic. As can be perceived from Fig. 7(a), the magnetization of the CZ is very low (almost zero) at room temperature and below up to 10 K it does not show any clear dependence on temperature, as it should be for a diamagnetic compound. The magnetic field dependent magnetization curves of the sample recorded at different temperatures are shown in Fig. 7(b). The susceptibility values are negative as can be seen from the slopes of the M − H plots, clearly indicating the diamagnetic behaviour of the sample. Susceptibility of the sample varies slightly with temperature. However, at a very low temperature (e.g. at 1.8 K), the sample develops a small ferromagnetic moment and the magnetization curve changes its slope from negative to positive near the magnetic field reversal region. This ferromagnetic contribution possibly comes from the impurities in the analytical grade zirconia sample.

The temperature and field-dependent magnetization curves of 10 h milled pure zirconia (PZ) sample presented in Fig. 8 clearly

indicate its ferromagnetic behaviour. The FC magnetization of the sample at 1.8 K is about 0.45 emu/g (Fig. 8(a)), which is quite high (100 times higher) in comparison to the un-milled pure zirconia (CZ). The FC curve bifurcates from the ZFC curve above room temperature (near 350 °C), due to an increase of ferromagnetic component in the sample in presence of magnetic field. The field dependent magnetization curves of the sample recorded at different temperatures are presented in Fig. 8(b). The field reversal region is expanded and shown in the inset of the figure for better visibility. As can be noticed, the sample reveals clear hysteresis loops at all the temperatures. Non-zero remnant magnetization (M_r) and coercive field (H_c) values are recorded at all the temperatures and their values at 1.8 K are given in the figure. While the saturation magnetization (M_s) of the sample is low at room temperature (300 K) and up to 100 K, it increases at lower temperatures. Presence of hysteresis at room temperature (300 K) clearly depicts that PZ exhibits room temperature ferromagnetism (RTFM). From oxygen partial pressure dependent M − H loop studies, Ning et al. [26]confirmed that the origin of RTFM in undoped zirconia is neither from any impurity nor associated with its monoclinic phase. The RTFM has been associated with the presence of oxygen vacancies in undoped zirconia thin films. In the review article by Ning and Zhang [27], they demonstrated significant enhancement of RTFM in ZrO_2 films due to an increase in oxygen vacancies. However, the ZrO_2 films studied by Ning et al. [26,27] were of undoped zirconia (with no intentionally added impurity) of oxygen vacancy-stabilized tetragonal phase without any trace of the cubic phase. The detailed Rietveld analysis of the PZ samples reported in this work confirms the formation of cubic phase in the Mn-stabilized samples, indicating both the structure/microstructure and oxygen vacancies in the zirconia lattice play significant roles on the RTFM behaviour of zirconia. In fact, the ferromagnetism exhibited by the PZ sample is governed from the oxygen vacant cubic ZrO_2 lattice. The oxygen vacancies in zirconia lattice act as cations and interact ferromagnetically with each other.

After confirming the ferromagnetic nature of 10 h milled pure zirconia nanoparticles, magnetic behaviour of Mn-stabilized zirconia nanoparticles can be discussed. Temperature and field dependent magnetizations of 5 mol% Mn-stabilized zirconia (5MZ) nanoparticles are shown in Fig. 9. The temperature-dependent magnetization (M-T) data were recorded under two different constant magnetic fields (Fig. 9(a)). As can be seen in the lower ZFC and FC curves of Fig. 9(a), even under a very low magnetic field, the ZFC and FC curves bifurcate below 375 K, indicating the onset of ferromagnetism. This nature is similar to undoped ZrO_2 sample
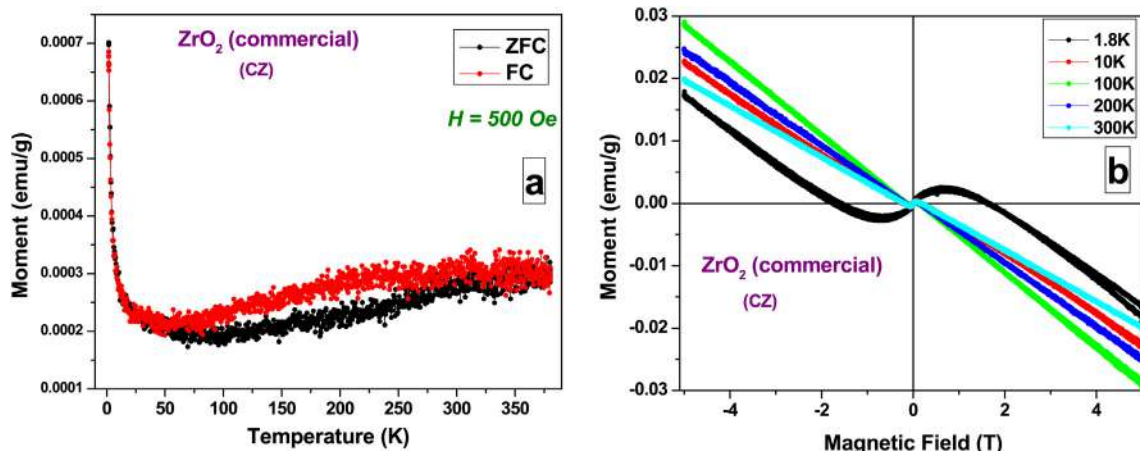

Fig. 7. (a) ZFC and FC curves and (b) magnetization curves at different temperatures for pure commercial analytical grade zirconia (CZ).
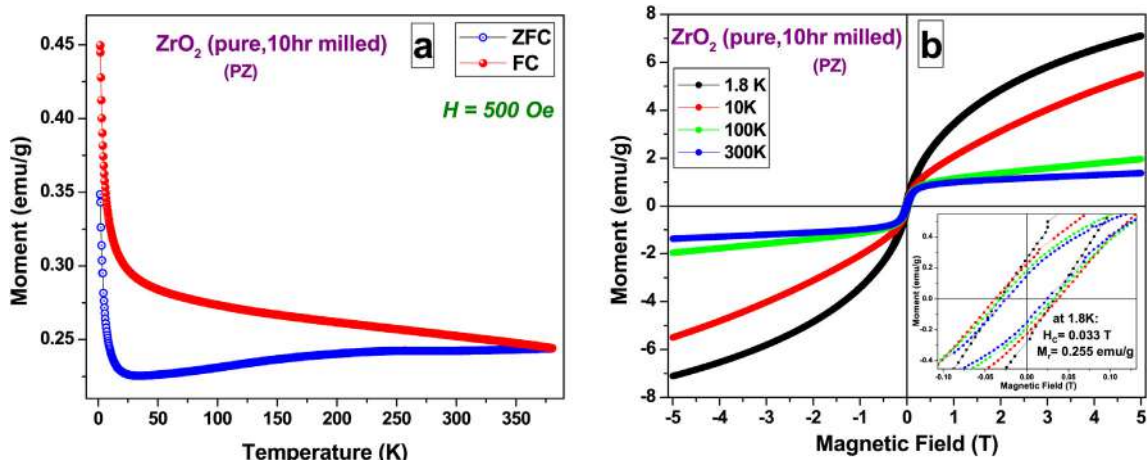
Fig. 8. (a) ZFC and FC curves and (b) magnetization curves at different temperatures for pure commercial analytical grade zirconia after 10 h of ball milling.
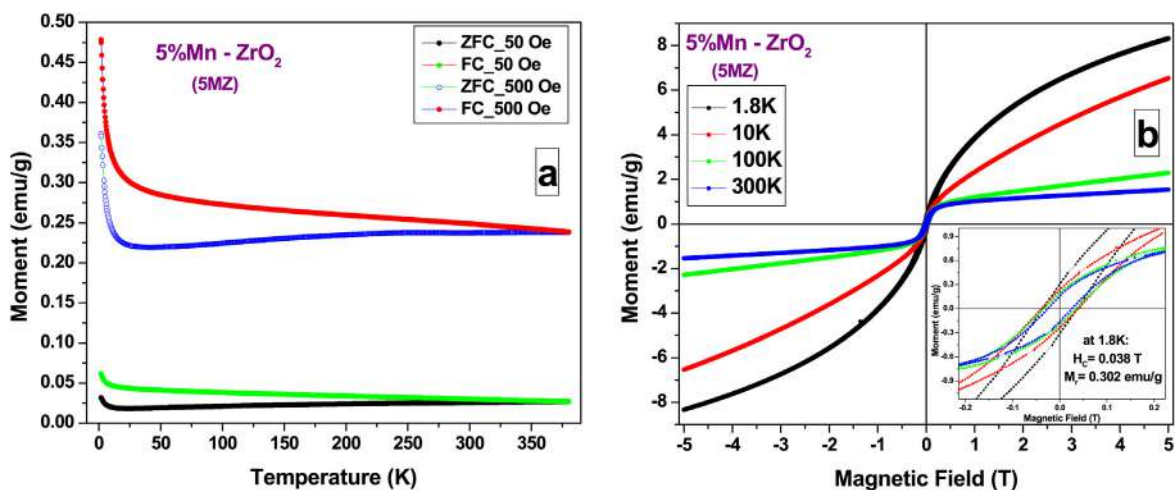

Fig. 9. (a) ZFC and FC curves and (b) magnetization curves at different temperatures for the 5 mol% Mn-stabilized zirconia obtained after 10 h of ball milling.

(PZ), as Mn is absolutely paramagnetic at this temperature. The ZFC and FC curves recorded under 500 Oe applied magnetic field are shown in the upper part of Fig. 9(a). The magnetization of the sample is now very similar to the undoped ZrO_2 sample (PZ), which increases with the decrease of temperature. The magnetization of the sample at 1.8 K is about 0.48 emu/g, compared to 0.45 emu/g for the undoped ZrO_2 sample (PZ). The field dependent magnetization curves recorded at four different temperatures in between 1.8 K and 300 K are shown in Fig. 9(b). It is observed from the inset of Fig. 9(b) that the sample reveals hysteresis loops with significant coercivity at all temperatures. The M − H curves are quite similar to that of undoped zirconia (PZ), except for the saturation magnetization values at low temperatures, which are little higher for the Mn-stabilized (5MZ) sample. This higher value of low-temperature magnetization can be attributed to a small increase in oxygen vacancy due to aliovalent Mn doping. Fig. 10 shows the M-T and M − H curves of 10 mol% Mn-stabilized ZrO_2 (10MZ) sample. It is evident that the basic nature of the M-T curves of the sample recorded under a 500 Oe applied magnetic field is same as of PZ and 5MZ, because of the origin and nature of magnetism are the same in these compounds. The ferromagnetic (FM) onset temperature is also the same for the two Mn-stabilized zirconia samples. However,

the magnetization values of the 10MZ sample are noticeably higher than that of 5MZ sample at all the temperatures. This can be well correlated to the sharp increase in C−ZrO_2 phase and a steep increase of oxygen vacancy concentration in the 10MZ (Fig. 3) sample. The downturn in the ZFC curves of 10 mol% Mn stabilized zirconia compounds can be due to the presence of competing for anti-ferromagnetic interaction between guest Mn atoms or between cationic oxygen vacancies. A similar increase in saturation magnetization can also be observed from the M − H plots of the sample presented in Fig. 10(b). It can be noticed (inset, Fig. 10(b)) that the remnant magnetization and coercive field at 1.8 K are much higher than the 5MZ sample. The M-T and M − H curves of 15MZ sample are shown in Fig. 11. Again, an increase in magnetization is observed in the ZFC and FC curves of the sample recorded under 500 Oe applied a magnetic field. The increase in magnetization is due to an increase in cubic phase fraction and oxygen vacancies. The low-temperature tip of the ZFC curve experiences a downturn, which may be due to the onset of anti-ferromagnetic interaction at that temperature. The saturation magnetization, coercive field and remnant magnetization at 1.8 K have also increased as can be seen from M − H curves plotted in Fig. 11(b). The inset of the figure shows enlarged hysteresis loops near field reversal region.
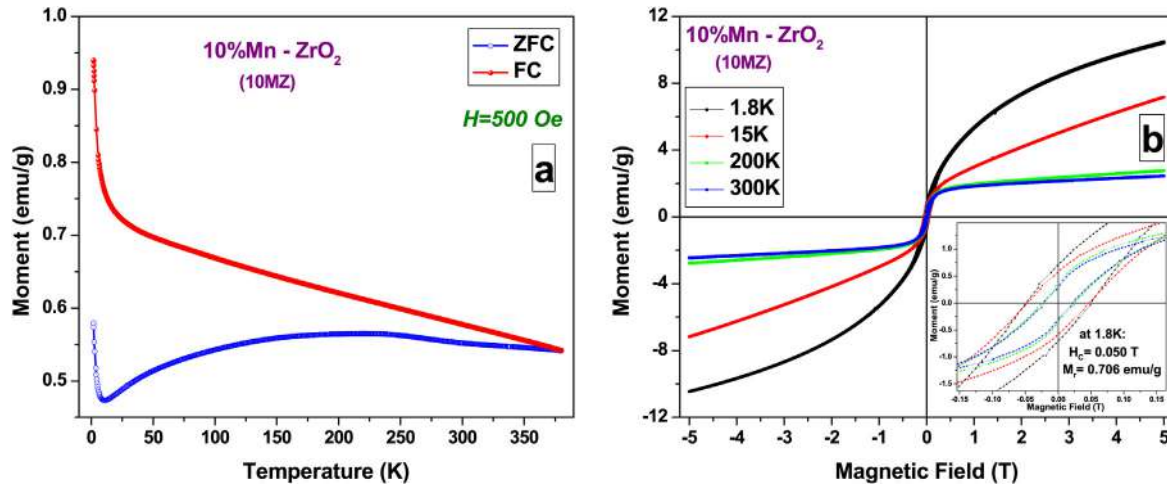
Fig. 10. (a) ZFC and FC curves and (b) magnetization curves at different temperatures for the 10 mol% Mn-stabilized zirconia obtained after 10 h of ball milling.
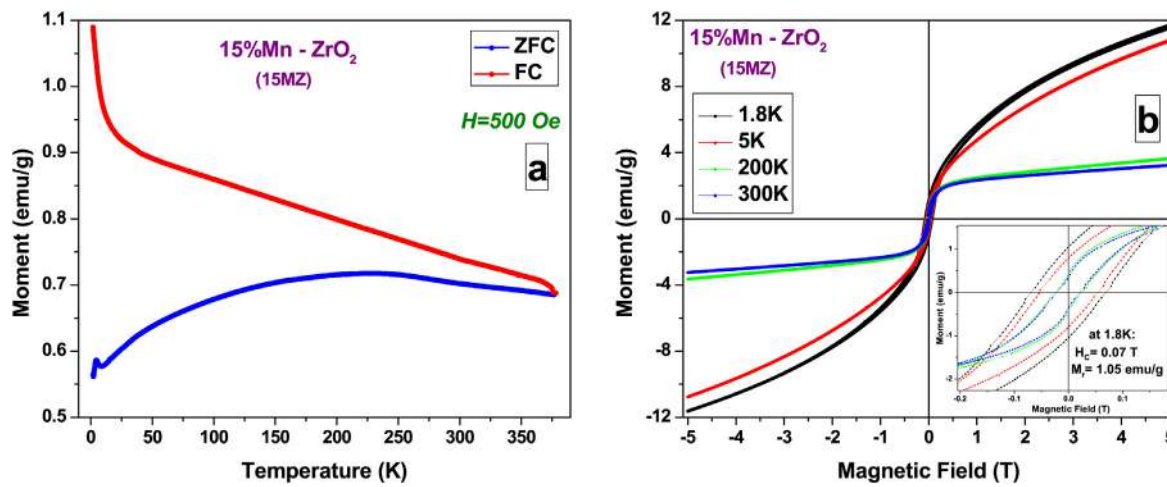

Fig. 11. (a) ZFC and FC curves and (b) magnetization curves at different temperatures for the 15 mol% Mn-stabilized zirconia obtained after 10 h of ball milling.
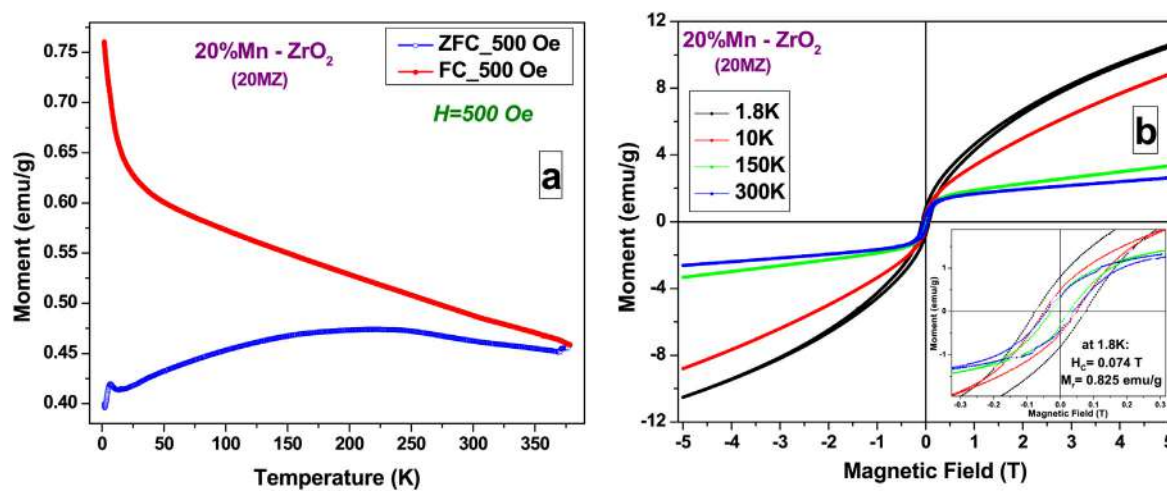

Fig. 12. (a) ZFC and FC curves and (b) magnetization curves at different temperatures for the 20 mol% Mn-stabilized zirconia obtained after 10 h of ball milling.

Temperature and field dependent magnetization of 20 mol% Mn−ZrO_2 (20MZ) is shown in Fig. 12. The bifurcation between ZFC and FC shows the clear presence of ferromagnetism in the compound at room temperature. However, the magnetization of the

sample is lower than the sample 15MZ, possibly due to the competing antiferromagnetic interaction between oxygen vacancies in high concentration and the dopant Mn atoms. The antiferromagnetic downturn is more pronounced at the low-temperature end of the ZFC curve. The M – H curves presented in Fig. 12(b) also point to a reduced magnetism in 20MZ sample.

As the solubility limit is reached at 20 mol% Mn, 25MZ and 30MZ represent two composite systems formed by 20 mol% Mn stabilized cubic ZrO_2 and metallic Mn. So the magnetic behaviour of 25MZ and 30MZ depends both on stabilized ZrO_2 and Mn metal. The M-T and M – H curves of 25 mol% Mn−ZrO_2 are shown in Fig. 13. A large increase in ZFC and FC magnetization can be observed in Fig. 13(a). The increase in magnetization can also be noted from the M – H curves in Fig. 13(b) at all the four measured temperatures. An enlarged view of the hysteresis loops near the field reversal region is given in the inset of Fig. 13(b). As the volume fraction of cubic zirconia phase and oxygen vacancies do not increase after 20 mol% Mn incorporation (Fig. 3), this increase in magnetization can be attributed to the contribution of the metallic Mn to the net magnetic moment of the sample. Formation of nanometric Mn clusters in Mn−ZrO_2 solid solution can contribute to the total magnetization of the stabilized zirconia in three possible ways, as has been described by Zippel et al. [24]. This are- (i) paramagnetic contribution from isolated Mn atoms, (ii) anti-ferromagnetic contribution due to direct coupling between nearby Mn atoms arising from Mn-Mn superexchange interaction and (iii) ferromagnetic contribution arising from double exchange interaction between Mn ions coupled via oxygen ions or oxygen vacancies. The ZFC curve up to 150 K is a signature of added paramagnetic contribution from Mn atoms to the ferromagnetic interaction in the oxygen-deficient cubic ZrO_2 lattice. Observed pronounced downturn in the curve below 100 K depicts the presence of strong antiferromagnetic interaction in the compound arising from the antiferromagnetic ordering of Mn atoms below 100 K. A large bifurcation between ZFC and FC curves also suggests the presence of magnetic anisotropy in the compound arising from structural anisotropy and antiferromagnetic spin alignment present in the compound [40].

Finally, the M-T curves of the 30MZ sample are presented in Fig. 14(a). The magnetization values have enhanced more due to the added amount of Mn atoms and their paramagnetic contribution. The ZFC curve shows a peak below 100 K which is possibly due to ferromagnetic double exchange interaction in Mn networks, mediated via oxygen atoms or oxygen vacancies. A huge downturn in ZFC curve, the high value of FC magnetization and large bifurcation between ZFC and FC at lower temperatures confirms the
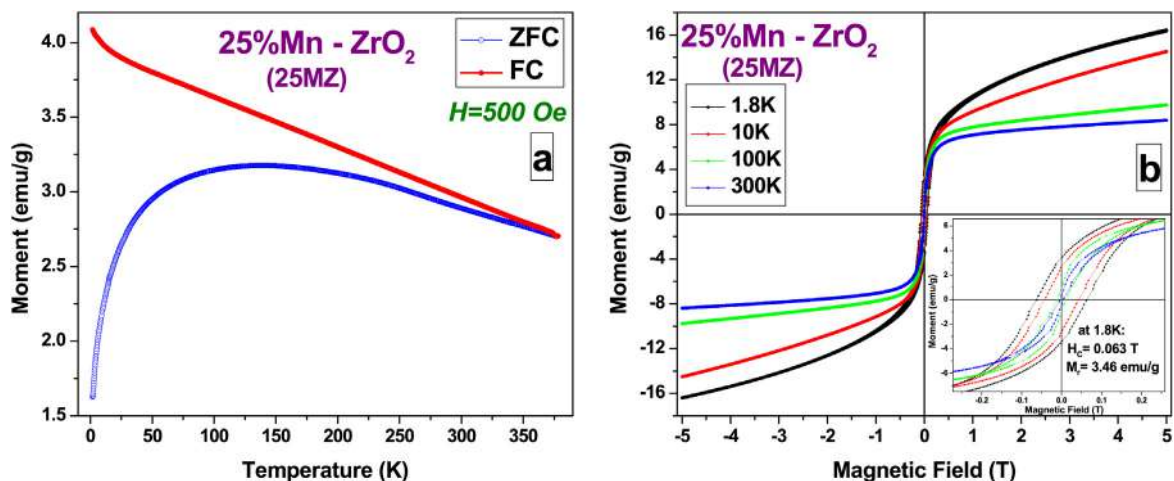

Fig. 13. (a) ZFC and FC curves and (b) magnetization curves at different temperatures for the 25 mol% Mn-stabilized zirconia obtained after 10 h of ball milling.
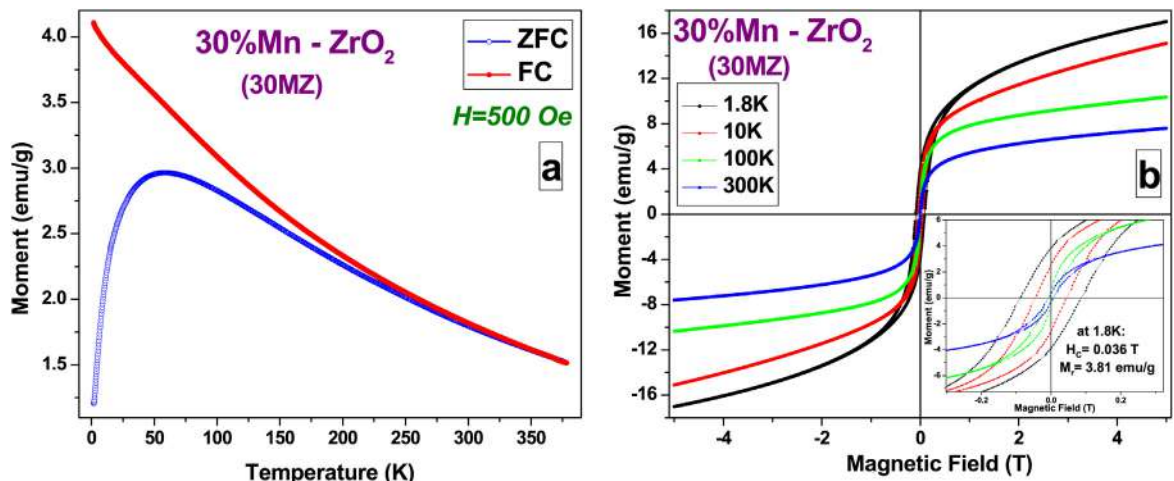

Fig. 14. (a) ZFC and FC curves and (b) magnetization curves at different temperatures for the 30 mol% Mn-stabilized zirconia obtained after 10 h of ball milling.

Table 2

Magnetic data of Mn alloyed ZrO_2 compounds at room temperature (300 K). Abbreviations: M — magnetization, M_s-saturation magnetization, M_r-remnant magnetization, H_c-coercive field.

Samples	Phases present (Volume fraction)	Oxygen Vacancy (c-ZrO_2)	M(ZFC) (emu/g)	M(FC) (emu/g)	M_s (emu/g)	M_r (emu/g)	H_c (T)
PZ	c-ZrO_2(77%), m-ZrO_2(23%)	10.2%	0.242	0.252	1.365	0.145	0.024
5MZ	c-ZrO_2(86%), m-ZrO_2(14%)	14.2%	0.237	0.249	1.541	0.158	0.025
10MZ	c-ZrO_2(87%), m-ZrO_2(13%)	21.6%	0.552	0.577	2.445	0.294	0.021
15MZ	c-ZrO_2(97.6%), m-ZrO_2(2.4%)	24.3%	0.702	0.739	3.229	0.361	0.021
20MZ	c-ZrO_2	26.6%	0.462	0.487	2.623	0.344	0.037
25MZ	c-ZrO_2(94.9%), Mn (5.1%)	26.9%	2.889	2.963	8.388	0.351	0.004
30MZ	c-ZrO_2(91.6%), Mn (8.4%)	27.1%	1.796	1.820	7.593	0.275	0.006

presence of antiferromagnetic superexchange interaction in Mn networks. The M – H curves of the sample recorded at different temperatures are presented in Fig. 14(b). The ferromagnetic nature of the sample is more clear from the hysteresis loops recorded at all the temperatures. It can be noticed that the separation between 100 K and 300 K hysteresis curves of the sample is more pronounced than 25MZ. This hints towards a ferromagnetic interaction near 100 K, possibly from double exchange interaction as also seen from the steep increase in ZFC curve below 100 K. The remnant magnetization values are particularly high at 1.8 K both for the 25MZ and 30MZ samples, indicating an extra contribution in magnetization from isolated Mn atoms. The room temperature magnetic data of all the samples are presented in Table 2 to elucidate the effect of Mn on room temperature ferromagnetic magnetic behaviour of ZrO_2 at a glance. From this table and from the magnetization plots, it can be inferred that room temperature ferromagnetism in undoped and doped zirconia materials greatly depends on oxygen vacancy. Rahman et al. [41] also established the dependence of ferromagnetism on oxygen vacancies in nano zirconia. The difference in ferromagnetic nature of tetragonal zirconia thin films studied in previous reports [26,27,41] to this report on mechanically alloyed homogeneous isotropic cubic zirconia nanoparticles suggests that the ferromagnetism in zirconia derivatives is also microstructure and morphology dependent. Very similar ferromagnetic nature of the undoped zirconia material to that of doped zirconia depicts that the magnetism in doped zirconia compounds is not dopant driven. Rather than contributing to magnetization, the role of the dopant is to increase oxygen vacancy in the sample, which actually drives the ferromagnetism. Magnetism in 25MZ and 30MZ compounds states that dopant in excess to the solubility limit can perturb the magnetization and change the magnetic nature due to its own magnetic behaviour.

4. Conclusion

Mechanical alloying of analytical grade monoclinic zirconia powder results in the formation of partially stabilized cubic ZrO_2, along with amorphous like phase and prevailing monoclinic phase. Addition of 5—30 mol% metallic Mn into monoclinic zirconia during mechanical alloying gradually stabilizes the cubic phase. Structural and microstructural parameters of all the mechanically alloyed powder samples are analyzed from Rietveld analysis. The solid solubility limit of Mn in cubic zirconia is found to be 20 mol%. A decrease in cubic lattice parameter up to 20 mol% and unchanged thereafter could be well correlated to the increase in oxygen vacancies in the Mn substituted ZrO_2 compound. All the alloyed compounds are found to be of nanometric dimension, with high lattice strain. The microstructure and phase formation is also confirmed by analysing HRTEM images. Analytical grade pure zirconia powder is found to be diamagnetic, except a small ferromagnetic term at very low temperature arising from the impurities in the as-received sample. Mechanically alloyed pure zirconia

sample is ferromagnetic even at room temperature. Thus, the ferromagnetism does not arise due to Mn doping. Instead, the ferromagnetic behaviour of stabilized zirconia compound arises due to the ferromagnetic interaction between the defects and oxygen vacancies present in cubic zirconia lattice. Ferromagnetic behaviour of the samples enhances as the Mn incorporation level increase sup to the solid solubility limit of 20 mol%. Beyond that, an anti-ferromagnetic term adds to the ferromagnetic contribution arising out of the isolated (unreacted) Mn phase.

References

[1] C. Xia, Electrolytes, in: J.W. Fergus, R. Hui, X. Li, D.P. Wilkinson, J. Zhang (Eds.), Solid Oxide Fuel Cells, CRC Press, Taylor and Francis Group, 2009, pp. 1—72.
[2] S.A. Steiner, T.F. Bauman, B.C. Bayer, J. Am. Chem. Soc. 131 (2009) 12144—12154.
[3] T.A. Cheema, G. Garnweitner, CrystEngComm 16 (2014) 3366—3375.
[4] D.C. Kundaliya, S.B. Ogale, S.E. Lofland, Nat. Mater. 3 (2004) 709—714.
[5] T.S. Herng, D.C. Qi, T. Berlijn, Phys. Rev. Lett. 105 (2010), 207201.
[6] P. Sharma, A. Gupta, K.V. Rao, Nat. Mater. 2 (2003) 673—677.
[7] S.A. Chambers, S. Thevuthasan, R.F. Farrow, Appl. Phys. Lett. 79 (2001) 3467—3469.
[8] J.Y. Kim, J.H. Park, B.G. Park, Phys. Rev. Lett. 90 (2003), 017401.
[9] K.A. Griffin, A.B. Pakhomov, C.M. Wang, Phys. Rev. Lett. 94 (2005), 157204.
[10] S.B. Ogale, R.J. Choudhary, J.P. Buban, Phys. Rev. Lett. 91 (2003), 077205.
[11] J. Hays, A. Punnoose, R. Baldner, Phys. Rev. B 72 (2005), 075203.
[12] C.B. Fitzgerald, M. Venkatesan, L.S. Dorneles, Phys. Rev. B 74 (2006), 115307.
[13] M. Venkatesan, C.B. Fitzgerald, J.M. Coey, Nature 430 (2004) 630.
[14] J.M. Coey, M. Venkatesan, P. Stamenov, Phys. Rev. B 72 (2005), 024450.
[15] J.M. Coey, M. Venkatesan, C.B. Fitzgerald, Nat. Mater. 4 (2005) 173—179.
[16] Z.Y. Chen, Z.Q. Chen, R.K. Pan, Chin. Phys. Lett. 30 (2013), 027804.
[17] N.H. Hong, J. Sakai, N. Poirot, Phys. Rev. B 73 (2006), 132404.
[18] C.D. Pemmaraju, S. Sanvito, Phys. Rev. Lett. 94 (2005), 217205.
[19] P. Dev, Y. Xue, P. Zhang, Phys. Rev. Lett. 100 (2008), 117204.
[20] H. Peng, J. Li, S.S. Li, Phys. Rev. B 79 (2009), 092411.
[21] S. Ostanin, A. Ernst, L.M. Sandratskii, P. Bruno, M. Dane, I.D. Hughes, J.B. Staunton, W. Hergert, I. Mertig, J. Kudrnovsky, Phys. Rev. Lett. 98 (2007), 016101.
[22] X. Jia, W. Yang, M. Qin, J. Li, J. Magn. Magn. Mater. 321 (2009) 2354—2358.
[23] G. Clavel, M.G. Willinger, D. Zitoun, N. Pinna, Eur. J. Inorg. Chem. (2008) 863—868.
[24] J. Zippel, M. Lorenz, A. Setzer, G. Wagner, N. Sobolev, P. Esquinazi, M. Grundmann, Phys. Rev. B 82 (2010), 125209.
[25] E. Albanese, A. Ruiz Puigdollers, G. Pacchioni, ACS Omega 3 (2018) 5301—5307.
[26] S. Ning, P. Zhan, Q. Xie, Z. Li, Z. Zhang, J. Phys. D Appl. Phys. 46 (2013), 445004, 5pp.
[27] S. Ning, Z. Zhang, J. Harbin Inst. Technol. 24 (2017) 1—10.
[28] A. Nandy, A. Dutta, S.K. Pradhan, Adv. Powder Technol. 28 (2017) 618—628.
[29] S. Saha, A. Nandy, A.K. Meikap, S.K. Pradhan, Physica B 479 (2015) 67—73.

[30] A. Nandy, C.S. Tiwary, A. Dutta, K. Chattopadhyay, S.K. Pradhan, Electrochim. Acta 170 (2015) 360–368.
[31] S. Bid, S.K. Pradhan, J. Appl. Crystallogr. 35 (2002) 517–525.
[32] H.M. Rietveld, J. Appl. Crystallogr. 2 (1969) 65–71.
[33] L. Lutterotti, P. Scardi, P. Maistrelli, J. Appl. Crystallogr. 25 (1992) 459–462.
[34] L. Lutterotti, LSI- a Computer Program for Simultaneous Refinement of Material Structure and Microstructure, Maud Version 2.26. http://www.ing.unitn.it/~maud/.
[35] M. Gateshki, V. Petkov, G. Williams, S.K. Pradhan, Y. Ren, Phys. Rev. B 71 (2005) 224107 1–9.
[36] R.D. Shannon, ActaCryst. A 32 (1976) 751.
[37] T. Kawada, N. Sakai, H. Yokokawa, M. Dokiya, Solid State Ionics 53–56 (1992) 418–425.
[38] J.M.D. Coey, Solid State Sci. 7 (2005) 660–667.
[39] J. Robertson, Eur. Phys. J. Appl. Phys. 28 (2004) 265–291.
[40] A. Nandy, A. Roychowdhury, D. Das, S.K. Pradhan, Powder Technol. 254 (2014) 538–547.
[41] Md A. Rahman, S. Rout, J.P. Thomas, D. Mc Gillivray, K.T. Leung, J. Am. Chem. Soc. 138 (36) (2016) 11896–11906.